applied sciences

MDPI

Article

Multi-Disciplinary Optimization of UV-C Filter for Air Disinfection

Igor Carli [1], Carlo Poloni [1], Alberto Clarich [2,*] and Rosario Russo [2]

[1] Department of Engineering and Architecture, University of Trieste, 34100 Trieste, Italy; igor.carli@studenti.units.it (I.C.); poloni@units.it (C.P.)
[2] Esteco SpA, 34149 Trieste, Italy; russo@esteco.com
* Correspondence: clarich@esteco.com; Tel.: +39-0403755548

Featured Application: To contain the diffusion of pathogens through air, a UV-C filter is optimized by CFD and ray tracing analysis guided by an MDO platform.

Abstract: Because of the recent COVID-19 pandemic, the problem of preventing and containing the diffusion of pathogens spread through air has become a main topic of research. The problem is particularly important for specific environments, such as dental or other medical practices, where the aerosol treatments in open-mouth patients, combined with closed and crowded rooms, raise the risk of infection. As an efficient countermeasure, in this study we propose a solution that is able to remove the risk at the source, through the aspiration of the aerosol and the neutralization of the bacterial load by means of a UV-C LED filter, which releases the sterilized air in the environment. To maximize the efficiency of the solution, in this study we performed a numerical multi-disciplinary optimization (MDO) of the filter, coupling numerical simulations of multiple disciplines (CFD and electromagnetics) by the process automation and optimization environment modeFRONTIER of ESTECO. Geometrical parameters of the filter are updated for each candidate solution proposed by the optimization algorithm, and their performance in terms of viral neutralization efficiency and air mass flow rate are evaluated by the simulations, until the optimal solution is found. The methodology and results of the study are presented.

Keywords: optimization; CFD; ray tracing simulation; UV-C filter; air pathogens neutralization

Citation: Carli, I.; Poloni, C.; Clarich, A.; Russo, R. Multi-Disciplinary Optimization of UV-C Filter for Air Disinfection. *Appl. Sci.* **2024**, *14*, 9901. https://doi.org/10.3390/app14219901

Academic Editors: Riccardo Rossi, Karl Jenkins and Tom-Robin Teschner

Received: 19 September 2024
Revised: 23 October 2024
Accepted: 26 October 2024
Published: 29 October 2024

1. Introduction

The development of ultraviolet germicidal irradiation (UVGI) originates in 1878, when Arthur Downes and Thomas Blunt found that sunlight, at shorter wavelengths, might restrict microbial growth [1]. As a consequence of this work, E. Duclaux identified, in 1885, variations in sunlight sensitivity among different bacterial species [2]. A few years later (1890), Robert Koch demonstrated the lethal effect of sunlight on Mycobacterium tuberculosis, discovering the great potential of UVGI to combat airborne diseases like tuberculosis [3].

The mutagenic effects of UV were first discovered in a 1914 study that observed metabolic changes in *Bacillus anthracis* when exposed to sublethal doses of UV [4]. In the late 1920s, Frederick Gates described the first bactericidal action spectra for *Staphylococcus aureus* and *Bacillus coli*, noting peak effectiveness at 265 nm [5]. This range corresponds to the absorption spectrum of nucleic acids, revealing DNA damage as the key factor in bacterial inactivation. This theory was consolidated by the 1960s through research demonstrating the ability of UV-C to form thymine dimers, which are responsible for microbial inactivation [6].

The methodic utilization of UVGI for air disinfection began in the mid-1930s. William F. Wells demonstrated in 1935 [7] that airborne infectious organisms, specifically aerosolized *B. coli* exposed to 254 nm UV, could be rapidly inactivated. Soon, this approach was extended

to several hospitals and infant wards using UVGI "light curtains", which were designed to prevent respiratory cross-infections [8].

Despite initial successes, the use of UVGI declined in the second half of the 20th century due to various reasons, in particular the rise of alternative infection control and prevention methods. However, recent events, like the appearance of drug-resistant bacteria and the COVID-19 pandemic, have renewed interest in UVGI for air disinfection [9].

Various engineering approaches to efficiently mitigating the presence of airborne pathogens inside building environments have therefore recently been investigated. Among these, we want to cite methodologies based on filtration, ultraviolet germicidal irradiation (UVGI) [10], and less common emerging methods, such as photocatalytic oxidation [11,12] and ionizing radiation [13]. The methodology that we focused on in the present study is the filtration of air within heating, ventilation, and air conditioning (HVAC) systems, supported by established classification and criteria (e.g., ANSI/ASHRAE Standard 52.2-1999, ISO 14644-1 1999) [14,15].

The particular case of UVGI disinfection that originally motivated our study is represented by dental or medical practices, where the combination of closed and non-aerated rooms with patients that cannot be protected by face masks during the medical operations significantly raises the infection risks for patients and medical operators.

In this study, therefore, we focused on a solution that aims to remove the risk at the source by the aspiration of the aerosol generated in the dental practice through a vented UV-C LED filter, which neutralizes the viral and bacterial load, releasing the sterilized air in the environment [16]. To minimize the impact of the solution on the working conditions and ergonomic necessities of the physician, the focus was on a design that is practical to use, that does not interfere with the physician's movements and vision, and that does not require particular attention or care during dental operations.

Since the efficiency of the pathogen neutralization is proportional to the intensity and time a microorganism is exposed to UV [17], it is required to perform a geometrical optimization of the filter, which maximizes the time the air flow carrying the bacterial load remains exposed to the UV radiation.

The MDO (multi-objective optimization) design of the filter was realized by coupling the numerical models with the optimization platform modeFRONTIER, which is used in various industrial fields, such as automotive and aeronautics, for the optimal design of products and systems according to the definition of the objectives and constraints. Optimization algorithms based on genetic algorithms and artificial intelligence guide the exploration of different candidate solutions by the automatic execution of several numerical simulations, until the design objectives are met.

The numerical models integrated in the MDO platform include CFD for the simulation of air flow across the filter and ray tracing to evaluate the intensity of UV radiation to which each particle transported by the air flow (as evaluated by particle tracking post-processing analysis over the CFD field) is exposed. By the combination of UV radiation intensity and exposure time on a given number of particles, it is possible to define the average dose absorbed by any pathogenic particle, as the objective of the optimization process to be maximized.

In the next sections we first describe the filter numerical models, and then we focus on the set-up and execution of the MDO optimization process, highlighting how the performance of the system was improved following this methodology.

2. Filter Modeling and Simulation

2.1. Combined Action of Air Ventilation and UV Radiation for Pathogen Neutralization

The effectiveness of germicidal UV depends on the duration a microorganism is exposed to UV, the intensity and wavelength of the UV radiation, and the presence of particles that can protect the microorganisms from UV [17].

Wavelengths between about 200 nm and 300 nm are strongly absorbed by nucleic acids, causing defects in pyrimidine dimers, which can prevent replication of necessary

proteins, resulting in the death or inactivation of the organism, as illustrated in Figure 1 [18].

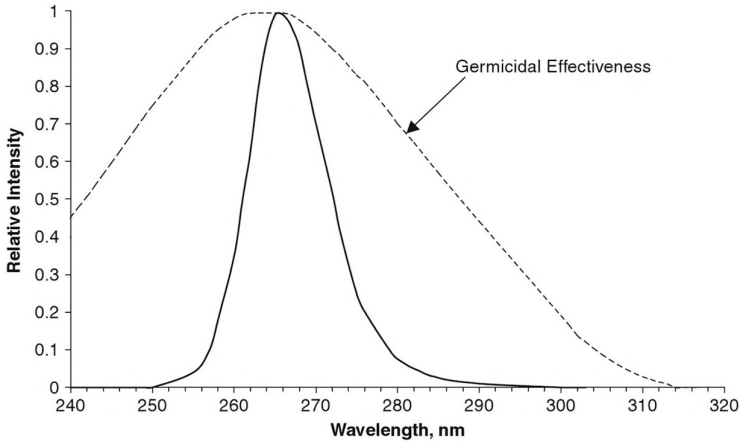

Figure 1. UV-C LED emitting 265 nm compared to the *E. coli* germicidal effectiveness curve. Adapted from paper cited in [18].

The effectiveness of UVGI increases when used in conjunction with fans and HVAC ventilation, which raise the exposition time of microorganisms to UV. The repeated circulation of the air ensures multiple passes so that the UV is effective against the highest number of microorganisms and can irradiate resistant microorganisms more than once to inactivate them.

The UV effectiveness can in fact be estimated by calculating the UV dose that is delivered to the microbial population. The UV dose is calculated as follows:

$$\text{UV dose } [\text{W}\cdot\text{s}/\text{m}^2] = \text{UV intensity } [\text{W}/\text{m}^2] \times \text{exposure time [s]} \quad (1)$$

In conclusion, to design an optimal UV-C filter, it is necessary to maximize the air flow rate and the exposure time of the air flow to the UV radiation.

2.2. Baseline Filter Performance

The baseline configuration of the filter we optimize in this work was designed by Stefano Fornasaro et al. [19] at University of Trieste in the *BAQLab* (Bioaerosol and Air Quality Laboratory).

The device geometry shown in Figure 2 [19] was originally patented (Italian patent n.0001401336) as a grease-removing device for industrial kitchens [20], capable of separating grease particles of 4–6 µm diameter. In the study reported in [19], the geometry was scaled down to interact with smaller particles and to fit with the available experimental apparatus. The internal walls of the prototype are made of highly reflective *POREX Virtek® PTFE*, which offers a certified reflectivity of 95–97% in the 200–300 nm wavelength range. On the opposite side of the device module, two UV-C LEDs are positioned and controlled with a dedicated adjustable power supply.

To evaluate the performance of the system for the neutralization of viral loads, the experimental setup was tuned with that previously designed for the understanding of the behavior of infectious SARS-CoV-2 in the aerosol phase, described by Zupin et al. in Ref. [21]. The aerosol allowed the generation of particles of different dimensions (0.5 µm and 2.5 µm) from the PBS solution enriched with a culture of non-pathogenic strain of *E. coli* (BL21-DE3), at two different concentrations: 10^7 and 10^8 CFU/mL.

The effect of different parameters was tested in [19] by an experimental campaign of 49 tests, which revealed that the most relevant factor was the total power of the two LEDs (maximum level: 300 mA), followed by the flow rate of the aerosol (maximum level: 50 L/min). In contrast, the particle size was revealed to be not significant in the study,

confirming that the method is efficient for every aerosol particle in the range from 0.5 to 2.5 µm.

After these results, we decided to optimize, by numerical simulations, the geometry of the filter, to obtain the maximum flow rate and the maximum exposure time, given the proper UV radiation.

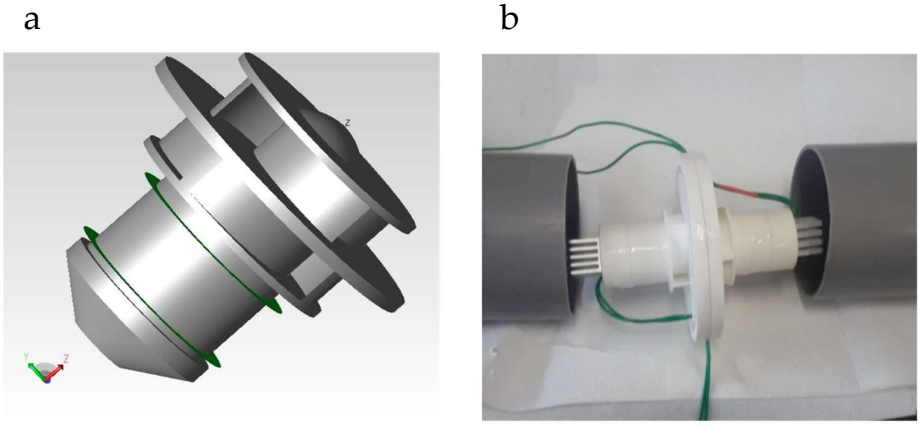

Figure 2. (**a**) Device geometry. (**b**) Assembled prototype used for the experimental testing. Adapted from paper cited in [19].

2.3. Filter Geometry Parameterization

The 3D geometry of the filter device studied in this work was modeled in CATIA v5, as illustrated in Figure 3a. In more detail, a total of eight geometrical dimensions were identified as design parameters, i.e., dimensions that can be changed in the optimization to obtain the optimal performance of the device.

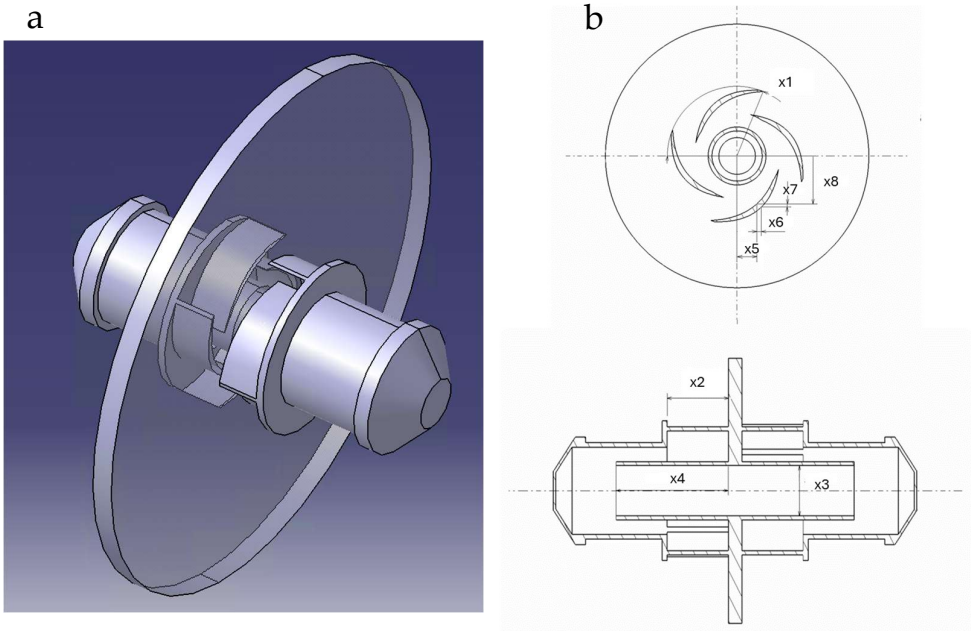

Figure 3. (**a**) Device geometry (Catia v5). (**b**) Definition of parameters.

Figure 3b indicates each parametric dimension with an ID number (x1, . . ., x8), which is then reported in Table 1 with the definition of the corresponding range of variation (minimum and maximum value of each dimension). More specifically, the parameters considered are the blade's height and angle of development, the internal radius of the hub and its length, and the coordinates of the median point of the external and internal profiles of the blades.

Table 1. Geometrical parameters and range of variation.

Parameter (Reference ID)	Lower Bound	Higher Bound
Blade_angle (x1)	45°	75°
Blade_height (x2)	15 mm	25 mm
Inner_radius (x3)	10 mm	20 mm
Z_length (x4)	25 mm	80 mm
X_inner (x5)	7.5 mm	12.5 mm
X_outer (x6)	0.1 mm	3 mm
Y_inner (x7)	22.5 mm	27.5 mm
Y_outer (x8)	0.1 mm	3 mm

2.4. CFD Simulation Model

Each updated CAD configuration is exported in a proper format (.CATPart file) to ANSYS Workbench, which generates the mesh and performs the CFD analysis. The mass flow rate entering the filter is one of the design parameters, and the selected range of variation is $[2.5 \times 10^{-4}: 16 \times 10^{-4}]$ kg/s, corresponding to [12.5 : 78.4] L/min.

To save computational time, an axial-symmetry model, corresponding to a quarter of the total volume, was defined (Figure 4). The inlet of the air flow is defined on the quarter circular surface at the left of Figure 4, while the outlet is defined at the end of the pipe (right, out of picture).

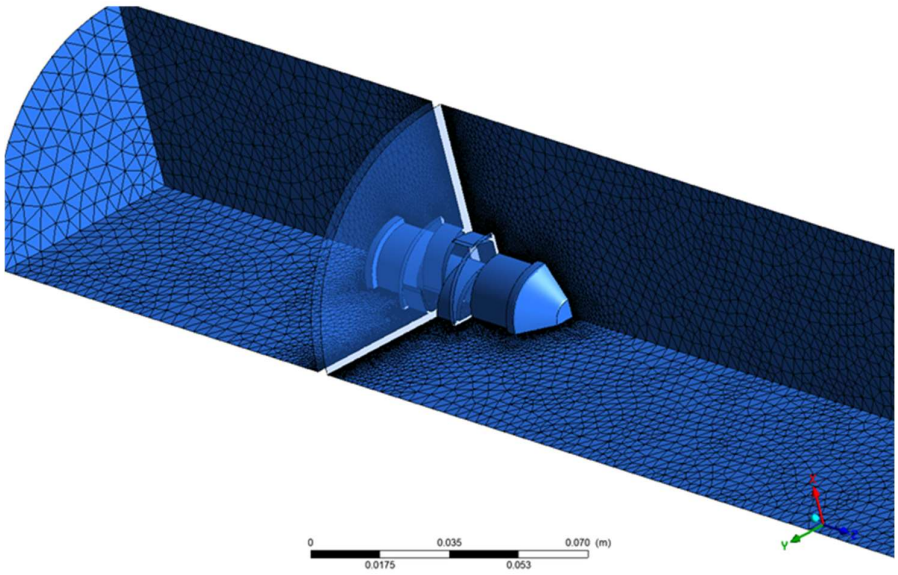

Figure 4. Air flow across the filter: mesh view.

The mesh is tetrahedral with prismatic layers defined on the wall (Figure 5), for a total of about 1.5 M elements. The Reynolds number of the flow is in the order of 1×10^4, which leads to the definition of a wall distance (minimum mesh size) of 0.5 mm, to yield a $Y+$ value < 5. For this mesh size, mesh independence studies revealed a proper convergence of the monitored quantity (maximum pressure and velocity on the median section of the filter; the errors for the selected mesh are lower than 1–2% with respect to a mesh of 3 M elements).

In the first stage, Navier–Stokes equations (Equation (2)) are defined for the stationary CFD analysis (using the solver Fluent of ANSYS 2024R1), implementing an *SST k-ω* turbulence model (Figure 6).

$$\frac{\partial}{\partial t}(\rho \boldsymbol{u}) + \nabla(\rho \boldsymbol{u} \cdot \boldsymbol{u}) = -\nabla p + \nabla \boldsymbol{\tau} + \rho \boldsymbol{g} \quad (2)$$

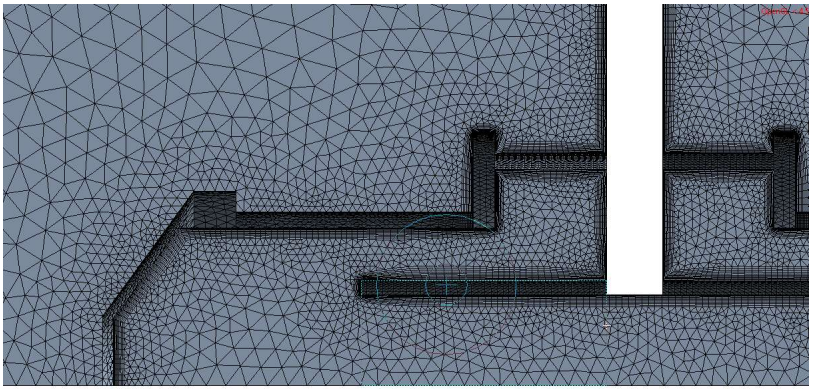

Figure 5. Air flow across the filter: mesh detail (the *z*-axis of the pipe is vertical).

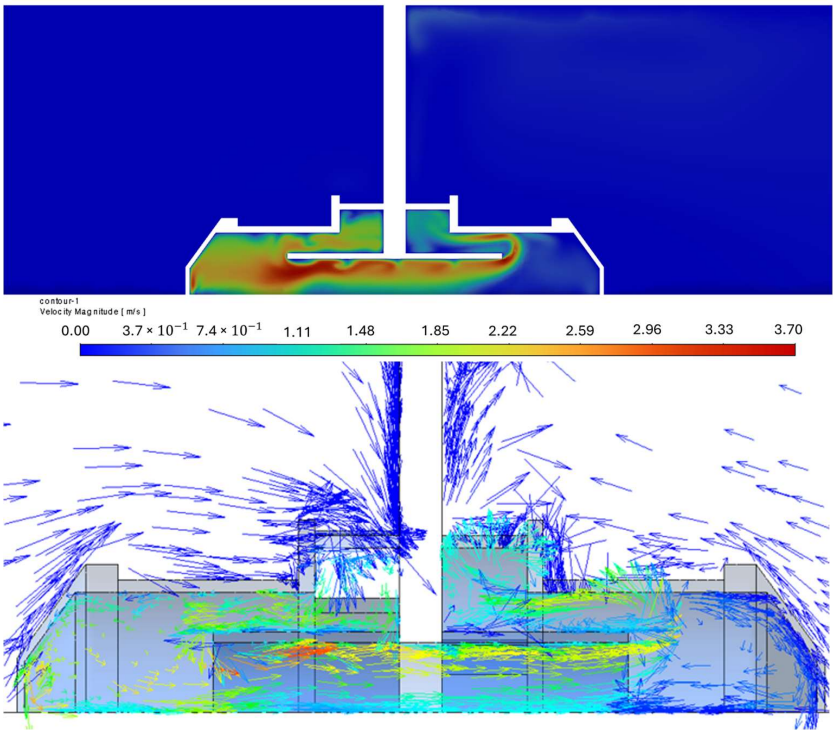

Figure 6. Air flow across the filter: velocity magnitude (**above**) and velocity vector (**below**) field.

In the second stage, on the basis of the flow field results across the filter, a particle tracking analysis was performed to understand how any pathogenic particle is transported by the air flow across the filter.

Various methodologies are available for particle tracking [22]; we adopted the one available in ANSYS Fluent, based on [23] the Basset–Boussineq–Oseen (BBO) equation (Equation (3)).

$$\frac{\pi}{6}\rho_P d_P^3 \frac{d\boldsymbol{U_P}}{dt} = 3\pi\mu d_P(\boldsymbol{U_f} - \boldsymbol{U_P}) - \frac{\pi}{6}d_P^3\nabla p + \frac{\pi}{12}\rho_f d_P^3 \frac{d}{dt}(\boldsymbol{U_f} - \boldsymbol{U_P}) + \rho_P d_P^3 \boldsymbol{g} \quad (3)$$

In Equation (3), the left term reports the rate of change in the particle momentum (ρ, d, and $\boldsymbol{U}$ are, respectively, the density, diameter, and velocity of the particle; the subscript P stands for particle). The right term reports the sum of the forces acting on the particle; the first term is the Stokes' drag (function of the fluid viscosity μ and velocity difference between particle, $\boldsymbol{U}_p$, and fluid, $\boldsymbol{U}_f$); the second term is the pressure gradient in the undisturbed flow; the third term is the added mass, which is an inertia forced induced by the accelerating particle moving a volume of surrounding fluid as it crosses through it; and the last term is the gravitational force.

In the original formulation of the BBO equation, an additional force, the Basset term, is also introduced to evaluate the viscous effects of the temporal delay in boundary layer development as the relative velocity changes with time. This term can, however, be discarded when, like in our case, the ratio of the density of the fluid (air) with the density of the particle is negligible.

For this study, it was decided to evaluate a total of 200 particle tracks. The starting position of the particles was defined at a uniform distance inside the inlet section of the filter, while the diameter of the particles was kept fixed to 1 µm, according to the analysis of the baseline performance described in Section 2.2 [19]. The final trajectories of the particles are therefore representative of the path a different pathogenic particle follows when crossing the filter.

2.5. UV Ray Tracing Simulation

The combination of CFD particle tracking and UV ray tracing simulations is used to evaluate how the changes in geometry parameters affect the device's performance and if the UV-C radiation intensity inside the device is sufficient to achieve a proper disinfection.

From the CFD analysis, as described in the previous paragraph, the trajectory of the particles through the device can be tracked. Figure 7a illustrates a sample of particle flow trajectories, colored by their velocity magnitude (m/s), for the baseline filter geometry. The residence time of each particle slightly changes between 0.37s and 0.41s.

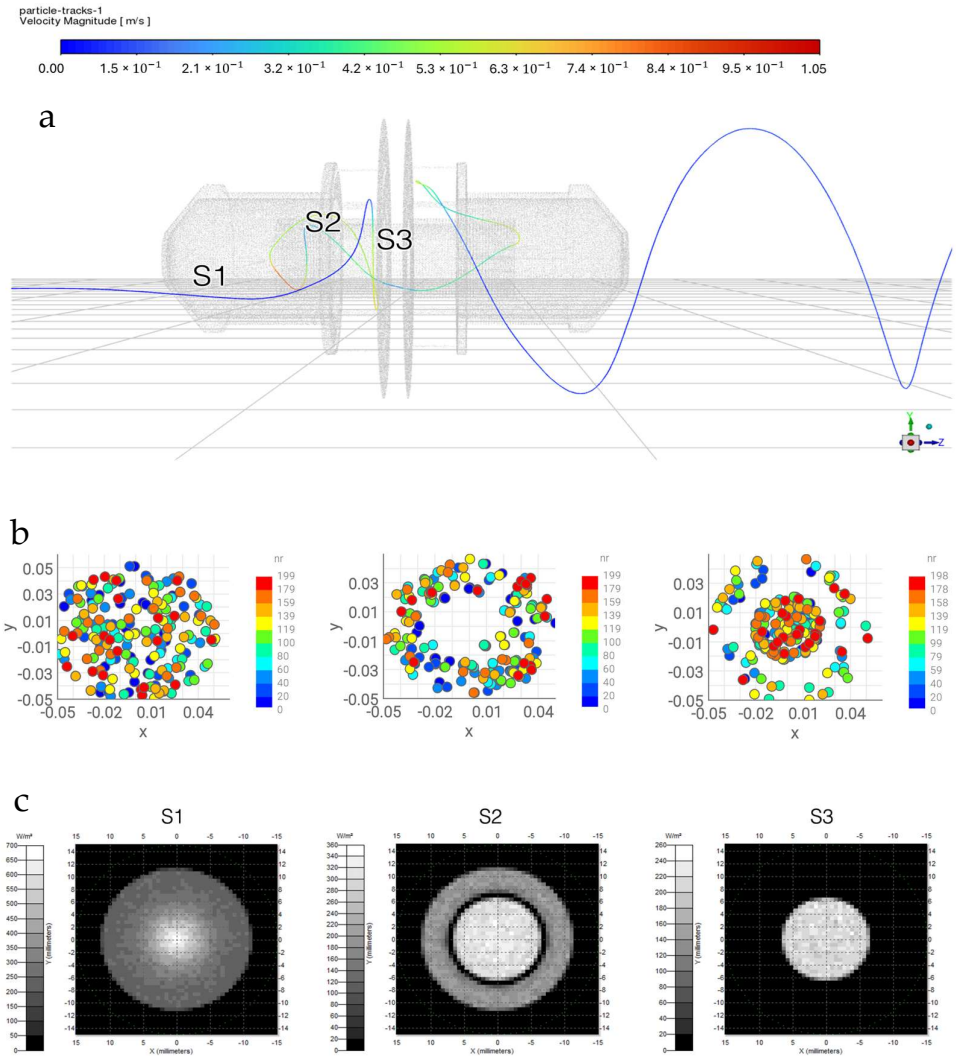

Figure 7. (**a**) Particle flow path sample. (**b**) Particle spatial distribution in 3 sections [m]. (**c**) Radiation intensity distributions in 3 sections [W/m^2]. Adapted from paper cited in [19].

For each design proposed in the optimization, the radiation intensity is evaluated by TracePro 2023 software in 14 different sections of the filter, equally spaced along the main z-axis. Figure 7b shows the X-Y position of each trajectory (colored by their ID number) for the baseline filter geometry in three key sections of the device (placed, respectively, at coordinates z1 = −6 cm, z2 = −1 cm, and z3 = 0 cm), while Figure 7c shows the UV radiation intensity [W/m^2] for the same three sections. For each of the 14 sections, a 100 × 100 matrix is defined, whose elements describe the UV intensity distribution on the (X, Y) plane.

By combining the radiation intensity with the particle trajectory, it is possible to compute the UV dose of radiation absorbed for each particle, as described by Equation (1). The trajectory of the particle is divided into N different timesteps, and at each timestep i the particle is associated with the closest section according to its axial position. The radiation absorbed in this timestep ($gi(x)$ in Equation (4)) is retrieved from the radiation intensity matrix corresponding to this section, at the (X, Y) position of the particle.

The total dose of radiation absorbed by the particle (Equation (4)) is finally obtained by summing the absorbed radiations in each timestep, multiplied by the delta time (ΔT) between two consecutive timesteps:

$$UV_i = \sum_i^N g_i\left(\vec{x}\right)\Delta T \tag{4}$$

3. Process Automation and Optimization

The CAD, CFD, and ray tracing simulation models were integrated in a single MDO (multi-disciplinary optimization) process automation workflow, within the optimization platform modeFRONTIER (Figure 8).

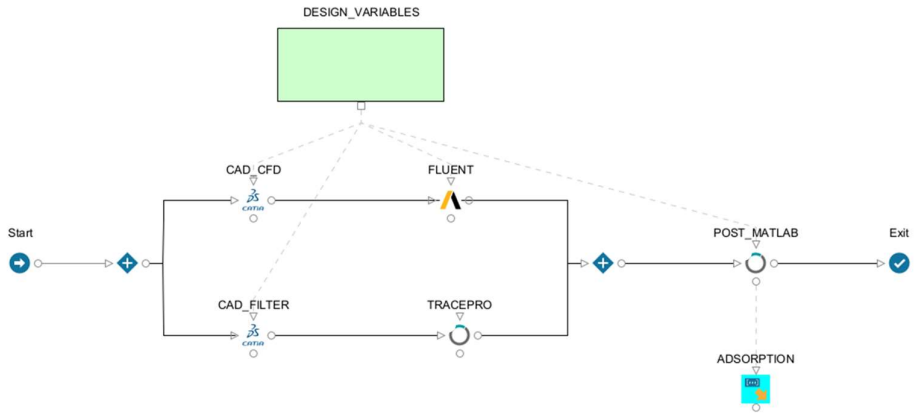

Figure 8. Process automation workflow for the MDO.

The process automation workflow is defined by a series of application nodes linked together with data and file nodes, with each one representing a different step of the process.

The logic of the process flow is divided into two paths, which are executed in parallel: from one side the application nodes for the CFD analysis, above, and from the other side, below, the application nodes for the ray tracing analysis.

In the first of the parallel paths, the first application node is the API-based connector interface with CATIA v5, which allows the automatic updating of the CAD model as a function of the values of the design parameters as described in Section 2.3, for each candidate design proposed by the optimization algorithm. This application is followed by another interface for Ansys, which rebuilds the mesh on the updated CAD model and executes the Fluent CFD simulation. The interface just replaces the original mesh model with the updated one, keeping the CFD boundaries and analysis settings unchanged.

In the second parallel path, the first application is a modified CAD node, which, as a function of the same design parameters, updates the geometry of the filter (note that the

first CAD model defines the CFD domain around the filter for the CFD analysis, while for the ray tracing analysis the filter geometry itself is needed). The updated geometry file is then transferred to the application, which executes the ray tracing analysis by the TracePro software.

When both simulation paths are executed, the results of the CFD analysis (the particle trajectories) and the results of the ray tracing analysis (the distribution of radiation intensity) are transferred to the last application of the workflow. This executes a MATLAB 2024a script, which computes the following objectives and constraints:

$$\overline{UV_i} = \sum_{i=1}^{N} \frac{UV_i}{N} \ [\mathrm{Ws/m^2}] \tag{5}$$

$$massflow = \int_{outlet} \rho V dS \left[\frac{kg}{s}\right] \tag{6}$$

$$\text{Min } UV_i \geq 25 \ [\mathrm{Ws/m^2}] \tag{7}$$

$$\sigma_{UV_i} = \sum_{i=1}^{N} \frac{\left(UV_i - \overline{UV_i}\right)^2}{\left(N-1\right)^2} < \ 0.667 \ \overline{UV_i} \tag{8}$$

Equation (5) is the absorption index defined as the first objective function to be maximized. It is computed as the average value of 200 different particle tracks of the ray absorption UV_i as expressed in Equation (4) for a single particle track (i.e., the product of the radiation intensity for exposure time). The value of this objective needs to be higher than 40 $\mathrm{Ws/m^2}$, as stated in [24], to achieve the necessary dose of inactivation.

Equation (6) indicates the second objective of the optimization, i.e., the maximization of the mass flow inside the UV-C filter, computed at the outlet section. This is necessary to maximize the air quantity that can be disinfected by the device.

In addition, two other constraints are defined by Equations (7) and (8): the minimum absorption index (min UV_i) among the different particle tracks must be higher than 25 $\mathrm{Ws/m^2}$ (to avoid any single particle having a too-low absorption index), and the standard deviation of the different particles index ($\sigma\ UV_i$) should be lower than 2/3 of the average value (to avoid a too-high dispersion of the particle efficiency distribution).

Once the objectives and constraints are defined and the process automation workflow is completed, the simulation and evaluation of the performances of each design proposed can be undertaken by the optimization proprietary algorithm (Pilopt) of modeFRONTIER. This algorithm combines genetic algorithms, gradient-based methodologies, and response surfaces to obtain the optimal solution with the lowest number of simulation evaluations.

4. Optimization Results

Before proceeding to the optimization process, a first DOE (Design of Experiments) series of designs was evaluated to analyze the significance of each parameter to the main objective of the study, i.e., the absorption index.

A DOE of 64 designs was evaluated using the Taguchi Orthogonal array scheme, which guarantees uniform coverage of the design space. A statistical analysis based on a PCE (polynomial chaos expansion) regression model was performed, revealing the cumulative sensitivity index (based on SOBOL indices) represented in Figure 9.

It follows that the height of the filter (z_height in Figure 3) is the parameter with the greatest effect on the absorption index, followed by the inner radius, blade angle, and the coordinates of the points controlling the blade curvature. Blade height, by contrast, revealed no significant effect, so this variable was disregarded in the optimization.

Figure 10 reports the results of the optimization after the execution of a total of 300 design simulations by the Pilopt algorithm.

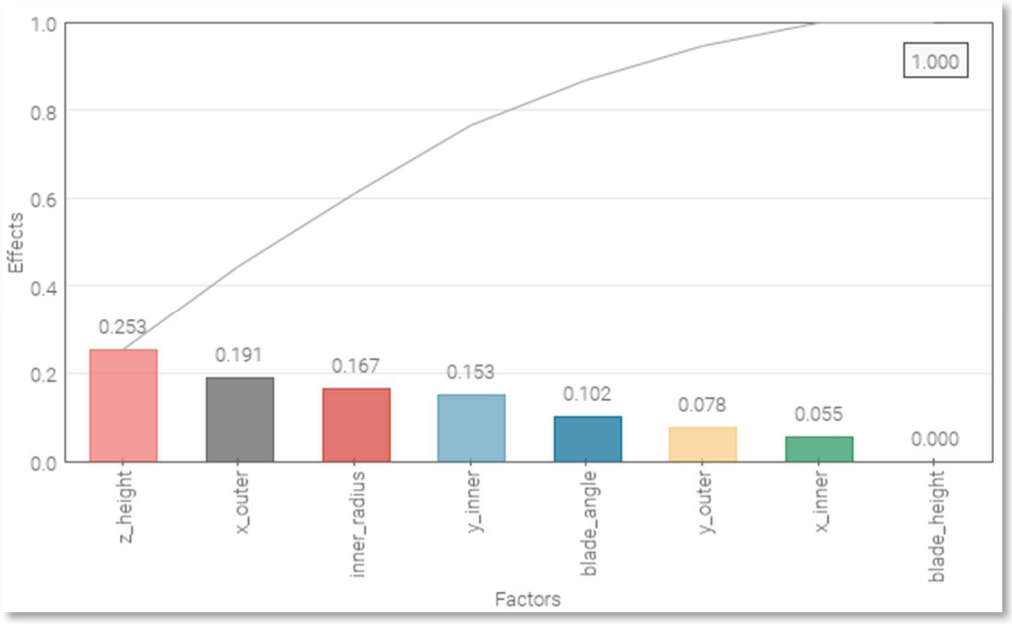

Figure 9. Effect table of design variables vs. absorption index.

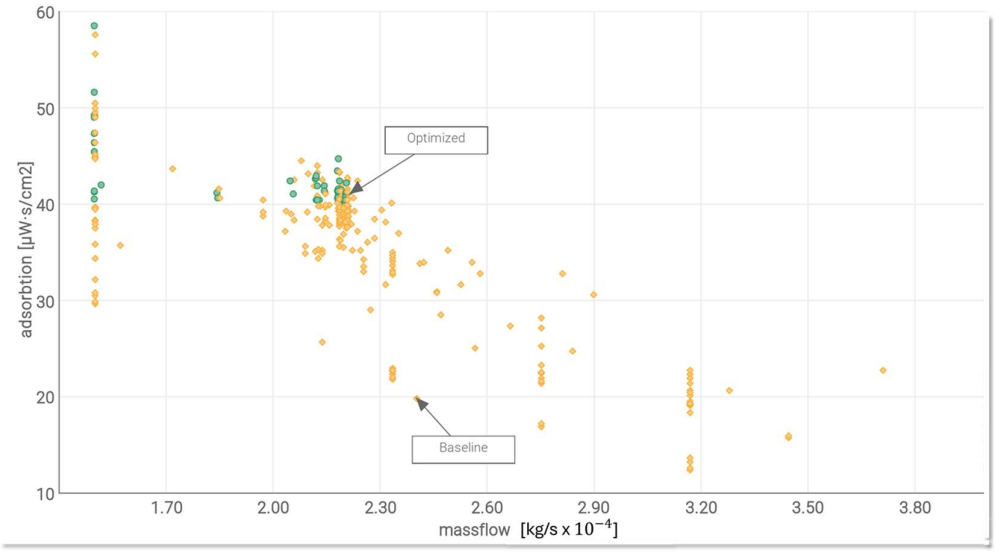

Figure 10. MDO results: mass flow vs. absorption index (feasible/unfeasible designs are represented in green/yellow color).

Each point of the chart reports a different design, where the yellow points represent unfeasible solutions (i.e., not respecting one or more of the constraints) and the green points represent feasible solutions. The two objectives of the optimization are reported in the abscissa (mass flow rate) and ordinates (absorption index) of the chart. Note that the mass flow reported on the *x*-axis corresponds to a quarter of the real flux in the filter due to the axial symmetry of the model.

Among the feasible solutions, the one indicated in Table 2 was selected as the optimal compromise among the several criteria. Table 2 reports a comparison of the optimal solution with the baseline.

Table 2. Geometrical parameters for baseline and optimal solution.

Parameter	Baseline	Optimal Solution
Blade_angle (x1)	60°	45°
Blade_height (x2)	20 mm	16.75 mm
Inner_radius (x3)	13 mm	17 mm
Z_height (x4)	39 mm	99.6 mm
X_inner (x5)	10 mm	10 mm
X_outer (x6)	2 mm	0.2 mm
Y_inner (x7)	25 mm	25 mm
Y_outer (x8)	2 mm	1.35 mm
Mass flow	2.5×10^{-4} kg/s	8.8×10^{-4} kg/s
Absorption efficiency	19.9 Ws/m^2	40.06 Ws/m^2
Minimum efficiency	17.25 Ws/m^2	26.76 Ws/m^2
Efficiency standard deviation	0.86 Ws/m^2	0.43 Ws/m^2

5. Conclusions

The application of MDO numerical optimization to the design of medical devices, such as an UV-filter for air disinfection, allows the efficiency of the product to be improved, while optimizing, at the same time, the computational and the human resources dedicated to the project.

Numerical simulation models from different disciplines, such as CFD and ray tracing, can be easily integrated in a MDO platform, which allows the automatic simulation of the different candidate solutions with the variation in the geometrical parameters. By selecting an opportune optimization strategy, the contrasting objectives and requirements can be optimized after the automatic execution of a few simulations without the need to remodel each design model by hand.

In the specific application illustrated in this paper, it was possible to optimize the baseline geometry of a UV-C filter medical device for air disinfection, with an important increase in the absorption coefficient of the pathologic load and of the air mass flow.

As future work, by considering a wider range of variation in the design parameters, it is expected that the performance of the device will be increased further. In addition, an experimental verification of the optimal geometry is foreseen.

Author Contributions: Conceptualization, C.P.; methodology, C.P., R.R. and A.C.; software simulations, I.C. and R.R.; validation, C.P., R.R. and A.C.; writing—original draft preparation, A.C.; writing—review and editing, C.P., R.R., I.C. and A.C.; supervision, A.C. and R.R.; project administration, C.P. All authors have read and agreed to the published version of the manuscript.

Funding: This research was partially funded by PRIN2022 "20229KTNRM".

Institutional Review Board Statement: Not applicable.

Informed Consent Statement: Not applicable.

Data Availability Statement: The raw data supporting the conclusions of this article will be made available by the authors on request.

Acknowledgments: The authors wish to thank Sabrina Semeraro, Stefano Fornasaro, and all the co-authors of the paper [11], which was the inspiration for the study reported in this contribution.

Conflicts of Interest: The authors declare the following competing financial interest: Carlo Poloni has patent #IT202000004255U1 issued to ESTECO SpA (80%) and University of Trieste (20%) for the device presented in this paper. The funders had no role in the design of the study; in the collection, analyses, or interpretation of data; in the writing of the manuscript; or in the decision to publish the results.

References

1. Downes, A.; Blunt, T.P. The Influence of Light upon the Development of Bacteria. *Nature* **1877**, *16*, 218. [CrossRef]
2. Duclaux, E. Influence de la luminére du soleil sur la vitalité des germes des microbes [Influence of sunlight on the vitality of germs of microbes]. *Comptes Rendus Hebd. Séances L'académie Sci. [Wkly. Minutes Sess. Acad. Sci.]* **1885**, *100*, 119–121. (In French)
3. Koch, R. Ueber bakteriologische Forschung [About bacteriological research]. In Proceedings of the Xth International Medical Congress, Berlin, Germany, 4–9 August 1890; Schwalbe, J., Gaffky, G., und Pfuhl, E., Eds.; A. Hirschwald: Berlin, Germany, 1890. (In German).
4. Henri, M.V. Variation du pouvoir abiotique des rayons ultraviolets avec leur longueur d'onde. *CR Seances Soc. Biol. Fil.* **1914**, *73*, 321–322.
5. Gates, F. A Study of the Bactericidal Action of Ultraviolet Light: I. The Reaction to Monochromatic Radiations. *J. Gen. Physiol.* **1929**, *13*, 231–248. [CrossRef] [PubMed]
6. Beukers, R.; Berends, W. Isolation and identification of the irradiation product of thymine. *Biochim. Biophys. Acta* **1960**, *41*, 550–551. [CrossRef] [PubMed]
7. Wells, W.F. On Air-Borne Infection. *Am. J. Epidemiol.* **1934**, *20*, 611–618. [CrossRef]
8. Sommer, H.E.; Stokes, J. Studies on air-borne infection in a hospital ward. *J. Pediatr.* **1942**, *21*, 569–576. [CrossRef]
9. Beggs, C.B.; Avital, E.J. Upper-room ultraviolet air disinfection might help to reduce COVID-19 transmission in buildings: A feasibility study. *PeerJ* **2020**, *8*, e10196. [CrossRef] [PubMed]
10. Nguyen, T.T.; Johnson, G.R.; Bell, S.C.; Knibbs, L.D. A Systematic Literature Review of Indoor Air Disinfection Techniques for Airborne Bacterial Respiratory Pathogens. *Int. J. Environ. Res. Public Health* **2022**, *19*, 1197. [CrossRef] [PubMed]
11. Vohra, A.; Goswami, D.Y.; Deshpande, D.A.; Block, S.S. Enhanced photocatalytic disinfection of indoor air. *Appl. Catal. B Environ.* **2006**, *64*, 57–65. [CrossRef]
12. Zacarías, S.M.; Manassero, A.; Pirola, S.; Alfano, O.M.; Satuf, M.L. Design and performance evaluation of a photocatalytic reactor for indoor air disinfection. *Environ. Sci. Pollut. Res.* **2021**, *28*, 23859–23867. [CrossRef] [PubMed]
13. Falagas, M.E.; Thomaidis, P.C.; Kotsantis, I.K.; Sgouros, K.; Samonis, G.; Karageorgopoulos, D.E. Airborne hydrogen peroxide for disinfection of the hospital environment and infection control: A systematic review. *J. Hosp. Infect.* **2011**, *78*, 171–177. [CrossRef] [PubMed]
14. NIOSH. *Guidance for Filtration and Air-Cleaning Systems to Protect Building Environments from Airborne Chemical, Biological, or Radiological Attacks*; U.S. Department of Health and Human Services, Public Health Service, Centers for Disease Control and Prevention, National Institute for Occupational Safety and Health: Washington, DC, USA, 2003. Available online: https://www.cdc.gov/niosh/docs/2003-136/ (accessed on 20 October 2024).
15. ASHRAE. *Filtration and Air Cleaning Summary*; ASHRAE: Peachtree Corners, GA, USA, 2023; Available online: https://www.ashrae.org/technical-resources/filtration-disinfection (accessed on 20 October 2024).
16. Ryan, K.; McCabe, K.; Clements, N.; Hernandez, M.; Miller, S.L. Inactivation of Airborne Microorganisms Using Novel Ultraviolet Radiation Sources in Reflective Flow-Through Control Devices. *Aerosol Sci. Technol.* **2010**, *44*, 541–550. [CrossRef]
17. Kim, D.-K.; Kang, D.-H. UVC LED Irradiation Effectively Inactivates Aerosolized Viruses, Bacteria, and Fungi in a Chamber-Type Air Disinfection System. *Appl. Environ. Microbiol.* **2018**, *84*, e00944-18. [CrossRef] [PubMed]
18. Kowalski, W. *Ultraviolet Germicidal Irradiation Handbook: UVGI for Air and Surface Disinfection*; Springer: Berlin/Heidelberg, Germany, 2009.
19. Fornasaro, S.; Semeraro, S.; Gaetano, A.S.; Licen, S.; Greco, E.; De Zorzi, R.; Russo, R.; Tenze, L.; Vinciguerra, G.; Poloni, C.; et al. Characterization and optimization of a novel UVC-LED aerodynamic device for airborne microbe viability abatement. *ACS ES&T Eng.* **2024**, *4*, 1600–1608.
20. Pediroda, V.; Carriglio, M.; Poloni, C. Design of Tridimensional Flow Separators by Optimization Techniques. In Proceedings of the Seventh International Conference on Flow Dynamics, Sendai, Japan, 1–3 September 2010.
21. Zupin, L.; Licen, S.; Milani, M.; Clemente, L.; Martello, L.; Semeraro, S.; Fontana, F.; Ruscio, M.; Miani, A.; Crovella, S.; et al. Evaluation of Residual Infectivity after SARS-CoV-2 Aerosol Transmission in a Controlled Laboratory Setting. *Int. J. Environ. Res. Public Health* **2021**, *18*, 11172. [CrossRef] [PubMed]
22. Brazhenko, V.; Qiu, Y.; Mochalin, I.; Zhu, G.; Cai, J.-C.; Wang, D. Study of hydraulic oil filtration process from solid admixtures using rotating perforated cylinder. *J. Taiwan Inst. Chem. Eng.* **2022**, *141*, 104578. [CrossRef]
23. Zhu, C.; Fan, L.-S. Chapter 18—Multiphase flow: Gas/Solid. In *The Handbook of Fluid Dynamics*; Johnson, R.W., Ed.; Springer: Berlin/Heidelberg, Germany, 1998.
24. Takamure, K.; Iwatani, Y.; Amano, H.; Yagi, T.; Uchiyama, T. Inactivation characteristics of a 280 nm Deep-UV irradiation dose on aerosolized SARS-CoV-2. *Environ. Int.* **2023**, *177*, 108022. [CrossRef] [PubMed]